INSTITUTE OF PHYSICS PUBLISHING INVERSE PROBLEMS

Inverse Problems **21** (2005) 1–11 doi:10.1088/0266-5611/21/1/001

Synthetic-aperture imaging from high-Doppler-resolution measurements

Brett Borden[1] **and Margaret Cheney**[2]

[1] Physics Department, Naval Postgraduate School, Monterey, CA 93943, USA
[2] Department of Mathematical Sciences, Rensselaer Polytechnic Institute, Troy, NY 12180, USA

Received 14 April 2004, in final form 4 October 2004
Published 9 November 2004
Online at stacks.iop.org/IP/21/1

Abstract

We develop the theory of radar imaging from data measured by a moving antenna emitting a single-frequency waveform. We show that, under a linearized (Born) scattering model, the signal at a given Doppler shift is due to a superposition of returns from stationary scatterers on a cone whose axis is the flight velocity vector. This cone reduces to a hyperbola when the scatterers are known to lie on a planar surface. In this case, reconstruction of the scatterer locations can be accomplished by a tomographic inversion in which the scattering density function is reconstructed from its integrals over hyperbolas. We give an approximate reconstruction formula and analyse the resolution of the resulting image. We provide a numerical shortcut and show results of numerical tests in a simple case.

1. Introduction

Standard synthetic-aperture radar imaging systems [23] transmit wideband waveforms, and the corresponding radar return signals are processed to synthesize the response from a sharp delta-like pulse. Such wideband waveforms are called *high-range-resolution* waveforms because their radar returns can be used to obtain accurate estimates of the distance (range) to a scatterer.

When a high-range-resolution system is used to image the scatterers on a flat surface, the radar return at each time t is a superposition of all the returns due to those scatterers positioned at distance $2t/c$ from the radar. The imaging problem can then be formulated [7, 1, 2, 11] in terms of reconstructing the scattering density function ρ from its integrals over all circles centred on the flight path of the antenna (see figure 1).

Radar systems can be designed, however, to operate in a complementary mode: instead of transmitting high-range-resolution pulses and estimating target range, they can transmit a high-Doppler-resolution waveform (a fixed-frequency waveform, also called a *continuous-wave* or *CW* waveform) and estimate the relative target velocity from the Doppler frequency shift of the return. For an antenna moving at a constant velocity over a flat surface, the return at a given Doppler shift is a superposition of all the returns due to scatterers with the same relative

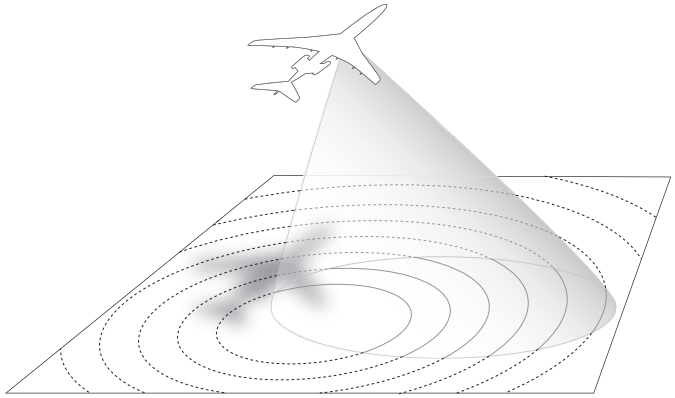

Figure 1. A high-range-resolution system.

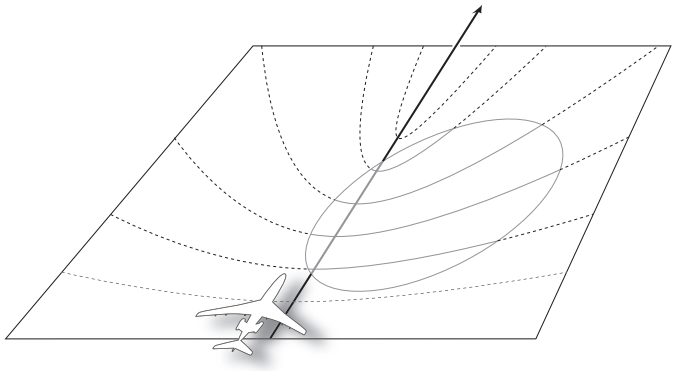

Figure 2. A high-Doppler-resolution system.

velocity, and all the scatterers with the same relative velocity lie on a certain hyperbola, called an *iso-Doppler* curve or *isodop*. This suggests a corresponding imaging approach: reconstruct the scattering density function ρ from its integrals over the iso-Doppler hyperbolas (see figure 2).

High-Doppler-resolution imaging systems (which we refer to as simply *Doppler imaging* systems) require only a relatively simple (inexpensive) transmitter and may thus have advantages over high-range-resolution systems in some situations. In addition, Doppler imaging systems may be useful in scenarios in which the radar signals must penetrate through a medium with a frequency-dependent attenuation.

The concept of Doppler imaging is not entirely new. The notion appears in [13]—in the context of a rotating target and stationary radar—to motivate the development of range-Doppler or inverse-synthetic-aperture imaging. Doppler-only imaging has also been applied to radar-based planetary imaging, but it appears that this work is restricted to very limited geometries [18]. The idea is also implicit in the theory of space-time adaptive processing [9]. Moreover, reconstruction of a scattering density function from its integrals over hyperbolas was developed, for wideband range-Doppler radar imaging, in [12]. Doppler imaging of a planar surface, however, does not seem to have been studied in its own right.

The purpose of this paper is to develop the theory of Doppler imaging for the case of a single sensor moving above a collection of scatterers lying on a surface. In section 2 we set forth our notation and a model for the received radar signal. In section 3 we specialize to the case of a flat earth and constant-velocity flight path. For this case, we develop an approximate image reconstruction algorithm.

2. Radar data

The basic physics behind radar detection is simple to understand. A time-varying voltage $s^{\text{in}}(t) \in \mathbb{C}$ is passed to a transmitting antenna where it activates a radiating electromagnetic field $\boldsymbol{E}^{\text{in}}(\boldsymbol{x}, t) \in \mathbb{C}^3$ defined at spatial position $\boldsymbol{x} \in \mathbb{R}^3$ and time t. This radiating field obeys the vector wave equation and interacts with radar *targets* by inducing time-varying charge distributions $\boldsymbol{j}(\boldsymbol{x}, t)$ on and within their support. In turn, these induced currents establish a response electromagnetic field $\boldsymbol{E}^{\text{sc}}(\boldsymbol{x}, t)$ (the 'scattered field') which radiates to a radar receiving antenna where it excites an echo signal voltage $s^{\text{sc}}(t)$ that is fed to the radar receiver. The radar system then uses the known function $s^{\text{in}}(t)$ and the measured function $s^{\text{sc}}(t)$ to estimate various properties of the target that are encoded in $\boldsymbol{j}(\boldsymbol{x}, t)$ (for example, the support of $\boldsymbol{j}$ can be used to determine the target's distance and bearing).

The details of the physics underlying the sequence $s^{\text{in}} \to \boldsymbol{E}^{\text{in}} \to \boldsymbol{j} \to \boldsymbol{E}^{\text{sc}} \to s^{\text{sc}}$ is usually quite complicated and, in practice, various simplifying approximations are applied to keep the analysis tractable.

2.1. The scattered field

The most common radar echo model is based on a linearized and polarization-insensitive scattering approximation to the electric or magnetic field integral equations. In this *ad hoc* approximation to the electromagnetic scattering problem, we consider only one electric field component, namely the one for which the antenna is designed to be sensitive. The *weak-scatterer* or *Born* approximation takes the induced current $\boldsymbol{j}$ to be proportional to the (scalar) $\tilde{\rho}\,\ddot{E}^{\text{in}}$, where $\tilde{\rho}$ is the *target reflectivity function,* and $\ddot{E}^{\text{in}}(\boldsymbol{z}, t)$ denotes the second time derivative of (one component of) the electric field incident upon the target. The Born-approximated scattered field is given by

$$E_B^{\text{sc}}(\boldsymbol{x}, t) \approx -\iint \frac{\delta(t - t' - |\boldsymbol{x} - \boldsymbol{z}|/c_0)}{4\pi\,|\boldsymbol{x} - \boldsymbol{z}|}\,\tilde{\rho}(\boldsymbol{z})\,\ddot{E}^{\text{in}}(\boldsymbol{z}, t')\,\mathrm{d}t'\mathrm{d}\boldsymbol{z} \tag{1}$$

where $E_B^{\text{sc}}(\boldsymbol{x}, t) \in \mathbb{C}$ denotes the designated component of the scattered electric field. The weak scatterer approximation is well documented in the literature (cf [3, 4, 13, 20, 23, 24] and references cited therein) and will not be further motivated here.

We assume that the radar emits a continuous wave at the fixed angular frequency ω_0. Then the incident field can be expressed in terms of the Green's function for the three-dimensional Helmholtz equation:

$$E^{\text{in}}(\boldsymbol{z}, t) = E_0(\widehat{\boldsymbol{z} - \boldsymbol{y}})\frac{\mathrm{e}^{-\mathrm{i}\omega_0(t - |\boldsymbol{z} - \boldsymbol{y}|/c)}}{4\pi\,|\boldsymbol{z} - \boldsymbol{y}|}, \tag{2}$$

where $\boldsymbol{y}$ denotes the phase centre of the transmitting antenna. Substitution into equation (1) yields

$$E_B^{\text{sc}}(\boldsymbol{x}, t) = \frac{\omega_0^2}{(4\pi)^2}\int \tilde{\rho}(\boldsymbol{z})\frac{\mathrm{e}^{-\mathrm{i}(\omega_0/c)(ct - |\boldsymbol{z} - \boldsymbol{y}| - |\boldsymbol{z} - \boldsymbol{x}|)}}{|\boldsymbol{z} - \boldsymbol{y}||\boldsymbol{z} - \boldsymbol{x}|}\,E_0(\widehat{\boldsymbol{z} - \boldsymbol{y}})\,\mathrm{d}\boldsymbol{z}. \tag{3}$$

Below we consider only the case where the transmit and receive antennas are co-located, have the same phase centres and travel along the flight path $\boldsymbol{x} = \boldsymbol{\gamma}(t)$. Moreover, we

assume that the scattering takes place in a thin region at the surface $z = \zeta(z_T)$, where $z_T = (z_1, z_2)$. Thus we write $\tilde{\rho}(z) = \rho(z_T)\delta(z - \zeta(z_T))$. We also introduce the notation: $\boldsymbol{R}(z_T, t) = \zeta(z_T) - \gamma(t)$; $R(z_T, t) = |\boldsymbol{R}(z_T, t)|$; and $\hat{\boldsymbol{R}}(z_T, t) = \boldsymbol{R}(z_T, t)/R(z_T, t)$. The field (3) is then

$$E_B^{\mathrm{sc}}(\gamma(t), t) = \frac{\omega_0^2}{(4\pi)^2} \int \rho(z_T) \frac{\mathrm{e}^{-\mathrm{i}\omega_0(t-2R(z_T,t))/c)}}{R^2(z_T, t)} E_0(\hat{\boldsymbol{R}}(z_T, t))\, \mathrm{d}z_T. \tag{4}$$

The measured signal voltage $s^{\mathrm{sc}}(t)$ arises from the interaction of E^{sc} with the antenna and we can write

$$s^{\mathrm{sc}}(t) = \frac{\omega_0^2}{(4\pi)^2} \int \rho(z_T) \frac{\mathrm{e}^{-\mathrm{i}\omega_0(t-2R(z_T,t))/c)}}{R^2(z_T, t)} W(\hat{\boldsymbol{R}}(z_T, t))\, \mathrm{d}z_T, \tag{5}$$

where W is a weighting factor accounting for the combined transmit and receive antenna patterns [21].

2.2. Correlation data

The radar receiver correlates the echo signal (5) with $\mathrm{e}^{-\mathrm{i}\omega t}$, which is a frequency-shifted version of the incident signal $s^{\mathrm{in}}(t) = \mathrm{e}^{-\mathrm{i}\omega_0 t}$, over a finite time window; in other words it measures the windowed Fourier transform. We denote by $\tilde{\psi}(t - \tau)$ the time windowing function centred at $t = \tau$; we write the (Fourier transform) frequency as $\omega = \omega_0\mu$. With this notation the radar data are

$$\begin{aligned}\eta(\tau, \mu) &= \int s^{\mathrm{sc}}(t)\, \mathrm{e}^{\mathrm{i}\omega_0\mu(t-\tau)} \tilde{\psi}(t - \tau)\, \mathrm{d}t \\ &= \frac{\omega_0^2}{(4\pi)^2} \iint \rho(z_T) \frac{\mathrm{e}^{-\mathrm{i}\omega_0(t-2R(z_T,t)/c)}}{R^2(z_T, t)} W(\hat{\boldsymbol{R}}(z_T, t))\, \mathrm{e}^{\mathrm{i}\omega_0\mu(t-\tau)} \tilde{\psi}(t - \tau)\, \mathrm{d}t\, \mathrm{d}z_T. \end{aligned} \tag{6}$$

Then, using the Taylor expansion

$$\gamma(t) = \gamma(\tau) + \dot{\gamma}(\tau)(t - \tau) + \cdots \tag{7}$$

to write

$$\begin{aligned} R(z_T, t) &= |\zeta(z_T) - \gamma(t)| = |\zeta(z_T) - \gamma(\tau) - \dot{\gamma}(\tau)(t - \tau) + \cdots| \\ &\approx R(z_T, \tau) - \hat{\boldsymbol{R}}(z_T, \tau) \cdot \dot{\gamma}(\tau)(t - \tau), \end{aligned} \tag{8}$$

in the exponent of (6), we obtain

$$\begin{aligned} \eta(\tau, \mu) \approx \frac{\omega_0^2}{(4\pi)^2} \iint \rho(z_T) &\frac{\mathrm{e}^{-\mathrm{i}\omega_0(t-2[R(z_T,\tau)-\hat{\boldsymbol{R}}(z_T,\tau)\cdot\dot{\gamma}(\tau)(t-\tau)]/c)}}{R^2(z_T, \tau)} \\ &\times W(\hat{\boldsymbol{R}}(z_T, t))\, \mathrm{e}^{\mathrm{i}\omega_0\mu(t-\tau)} \tilde{\psi}(t - \tau)\, \mathrm{d}t\, \mathrm{d}z_T. \end{aligned} \tag{9}$$

Finally, in (9) we make the change of variables $t' = t - \tau$ to obtain

$$\eta(\tau, \mu) \approx \iint \mathrm{e}^{-\mathrm{i}\omega_0 t'(1-\mu+2\hat{\boldsymbol{R}}(z_T,\tau)\cdot\dot{\gamma}(\tau)/c)} \tilde{A}(z_T, t', \tau)\, \mathrm{d}t' \rho(z_T)\, \mathrm{d}z_T \tag{10}$$

where $t' = t - \tau$ and

$$\tilde{A}(z_T, t', \tau) = \frac{\omega_0^2\, \mathrm{e}^{-\mathrm{i}\omega_0(\tau-2R(z_T,\tau)/c)} \tilde{\psi}(t')}{(4\pi R(z_T, \tau))^2} W(\hat{\boldsymbol{R}}(z_T, t' + \tau)). \tag{11}$$

We see that the t' integration results in an approximate delta function along the curve formed by the intersection of the earth's surface with the constant-Doppler cone $\mu - 1 = 2\hat{\boldsymbol{R}}(\tau, \boldsymbol{x}_T) \cdot \dot{\gamma}(\tau)/c$. When the earth's surface is a flat plane, this curve is a hyperbola.

We use the dimensionless parameter $\beta = \omega_0 t'$ to write $A(\boldsymbol{z}_T, \beta, \tau) = \tilde{A}(\boldsymbol{z}_T, t', \tau)$ and

$$\varphi(\beta, \boldsymbol{z}_T, \tau, \mu) = \beta[1 - \mu + 2\hat{\boldsymbol{R}}(\boldsymbol{z}_T, \tau) \cdot \dot{\boldsymbol{\gamma}}(\tau)/c] \tag{12}$$

so that (10) is

$$\eta(\tau, \mu) = \iint A(\boldsymbol{z}_T, \beta, \tau)\, \mathrm{e}^{-\mathrm{i}\varphi(\beta, \boldsymbol{z}_T, \tau, \mu)}\, \mathrm{d}\beta \rho(\boldsymbol{z}_T)\, \mathrm{d}\boldsymbol{z}_T. \tag{13}$$

3. The case of a straight flight path and flat earth

We choose coordinates so that the flight path is along the z_1 axis: $\boldsymbol{\gamma}(\tau) = (v\tau, 0, H)$, and we assume that the radar is operating in strip-map mode, meaning that the antenna beam is fixed and side-looking. We assume that the antenna beam illuminates the region $|z_1 - v\tau| \lesssim \epsilon$. The phase (12) is thus

$$\begin{aligned}\varphi(\beta, \boldsymbol{z}_T, \tau, \mu) &= \beta \left[1 - \mu + \frac{2v}{c} \frac{z_1 - v\tau}{\sqrt{(z_1 - v\tau)^2 + z_2^2 + H^2}} \right] \\ &= \beta \left[1 - \mu + \frac{2v/c}{\sqrt{z_2^2 + H^2}} (z_1 - v\tau) + O\big((z_1 - v\tau)^2\big) \right] \end{aligned} \tag{14}$$

where in the second line of (14) we have done a Taylor expansion about the point $z_1 = v\tau$. We use the notation $\tilde{\mu} = \mu - 1$ and use ϕ for the approximate form of the phase:

$$\phi(\beta, \boldsymbol{z}_T, \tau, \tilde{\mu}) = \beta \left[-\tilde{\mu} + \frac{2v/c}{\sqrt{(z_2/H)^2 + 1}} \left(\frac{z_1}{H} - \frac{v\tau}{H} \right) \right]. \tag{15}$$

The leading-order contribution to η comes from the critical set $\partial\phi/\partial\beta = 0$, which, in this approximation, is a straight line in the $\tilde{\mu}$–τ plane. If instead of τ we use the dimensionless variable $\tilde{\tau} = v\tau/H$, then we find that the straight line in the $\tilde{\mu}$–$\tilde{\tau}$ pane has $\tilde{\tau}$-intercept z_1/H and slope $-2(v/c)((z_2/H)^2 + 1)^{-1/2}$. We note that z_1 can be found from the $\tilde{\tau}$-intercept, and z_2 from the slope.

3.1. Image formation

We form an image by backprojection:

$$I(\boldsymbol{y}_T) = \iiint \mathrm{e}^{\mathrm{i}\phi(\beta, \boldsymbol{y}_T, \tau, \tilde{\mu})} B(\beta, \boldsymbol{y}_T, \tau, \tilde{\mu})\, \mathrm{d}\beta \eta(\tau, \tilde{\mu})\, \mathrm{d}\tilde{\mu}\, \mathrm{d}\tau \tag{16}$$

where B is to be determined below.

To determine the degree to which the image I reproduces ρ, we insert (13) into (16) and perform a stationary phase reduction in $\tilde{\mu}$ and one of the β variables. This results in

$$I(\boldsymbol{y}_T) = \int K(\boldsymbol{y}_T, \boldsymbol{z}_T) \rho(\boldsymbol{z}_T)\, \mathrm{d}\boldsymbol{z}_T, \tag{17}$$

where the point spread function K is given by

$$\begin{aligned} K(\boldsymbol{y}_T, \boldsymbol{z}_T) = \iint \exp &\left(\mathrm{i}\beta \frac{2v}{c} \left[\frac{y_1 - v\tau}{\sqrt{y_2^2 + H^2}} - \frac{z_1 - v\tau}{\sqrt{z_2^2 + H^2}} \right] \right) A(\boldsymbol{z}_T, \tau) \\ &\times B(\beta, \boldsymbol{y}_T, \tau, \mu(\boldsymbol{y}_T, \tau)) \psi(\beta)\, \mathrm{d}\beta\, \mathrm{d}\tau \end{aligned} \tag{18}$$

and where $\mu(\boldsymbol{y}_T, \tau) = -(2v/c)(y_1 - v\tau)\left(y_2^2 + H^2\right)^{-1/2}$. We would like to choose B so that $K(\boldsymbol{y}_T, \boldsymbol{z}_T) = \delta(\boldsymbol{y}_T - \boldsymbol{z}_T) = (2\pi)^{-2}\int \mathrm{e}^{-\mathrm{i}(\boldsymbol{y}_T - \boldsymbol{z}_T)\cdot\boldsymbol{\xi}}\,\mathrm{d}\boldsymbol{\xi}$.

The leading-order contributions to (18) come from the critical points of (18), which are determined by

$$0 = \frac{\partial\phi}{\partial\beta} \propto \frac{y_1 - v\tau}{\sqrt{y_2^2 + H^2}} - \frac{z_1 - v\tau}{\sqrt{z_2^2 + H^2}}, \qquad 0 = \frac{\partial\phi}{\partial\tau} \propto \frac{1}{\sqrt{y_2^2 + H^2}} - \frac{1}{\sqrt{z_2^2 + H^2}}. \tag{19}$$

These equations have solutions only when $(y_1, y_2) = (z_1, \pm z_2)$, which implies that the only artefacts are the usual left–right ones. (And these artefacts can be avoided by a judicious choice of $W(\hat{\boldsymbol{R}}, \tau)$.)

In (18), we expand the phase using the identity

$$f(\boldsymbol{z}_T) - f(\boldsymbol{y}_T) = (\boldsymbol{z}_T - \boldsymbol{y}_T)\int_0^1 \nabla f(\boldsymbol{y}_T + \lambda(\boldsymbol{z}_T - \boldsymbol{y}_T))\,\mathrm{d}\lambda \approx (\boldsymbol{z}_T - \boldsymbol{y}_T)\cdot\nabla f(\boldsymbol{y}_T) \tag{20}$$

applied to $f(\boldsymbol{y}_T) = (y_1 - v\tau)\left(y_2^2 + H^2\right)^{-1/2}$. We then make the change of variables

$$(\beta, \tau) \to \boldsymbol{\xi} = (2\beta v/c)\nabla f(\boldsymbol{y}_T) = \beta\frac{2v}{c}\left(\frac{1}{\sqrt{y_2^2 + H^2}}, \frac{-(y_1 - v\tau)y_2}{\left(y_2^2 + H^2\right)^{3/2}}\right)^{\mathrm{T}} \tag{21}$$

where the superscript T denotes transpose. This converts (18) into

$$K(\boldsymbol{y}_T, \boldsymbol{z}_T) = \int \mathrm{e}^{\mathrm{i}(\boldsymbol{z}_T - \boldsymbol{y}_T)\cdot\boldsymbol{\xi}} A(\boldsymbol{z}_T, \tau) B(\beta, \mu(\boldsymbol{y}_T, \tau), \tau, \boldsymbol{y}_T)\psi(\beta)\left|\frac{\partial(\beta, \tau)}{\partial\boldsymbol{\xi}}\right|\mathrm{d}\boldsymbol{\xi} \tag{22}$$

where now β and τ are understood to refer to $\beta(\boldsymbol{\xi})$ and $\tau(\boldsymbol{\xi})$. The Jacobian in (22) is the reciprocal of

$$\left|\frac{\partial\boldsymbol{\xi}}{\partial(\beta, \tau)}\right| = \frac{4v^2\beta}{c^2}\begin{vmatrix} \dfrac{1}{\sqrt{y_2^2 + H^2}} & 0 \\ \dfrac{-(y_1 - v\tau)y_2}{\left(y_2^2 + H^2\right)^{3/2}} & \dfrac{vy_2}{\left(y_2^2 + H^2\right)^{3/2}} \end{vmatrix} = \frac{4v^3\beta y_2}{c^2\left(y_2^2 + H^2\right)^2}. \tag{23}$$

From (22), we see that B should be chosen according to

$$B(\beta, \mu, \tau, \boldsymbol{y}_T) = \frac{\chi(\beta, \tau, \boldsymbol{y}_T)\left|\frac{\partial\boldsymbol{\xi}}{\partial(\beta, \tau)}\right|}{(2\pi)^2 A(\boldsymbol{y}_T, \tau)\psi(\beta)} \tag{24}$$

where χ is a cutoff function that prevents division by zero in (24). With this choice of B, (22) becomes

$$K(\boldsymbol{y}_T, \boldsymbol{z}_T) = \frac{1}{(2\pi)^2}\int_{\Xi_y} \mathrm{e}^{\mathrm{i}(\boldsymbol{z}_T - \boldsymbol{y}_T)\cdot\boldsymbol{\xi}}\,\mathrm{d}\boldsymbol{\xi} \tag{25}$$

where the integration is over the set Ξ_y of $\boldsymbol{\xi}$ swept out according to (21) as τ and β range over the data collection region for the point $\boldsymbol{y}_T$.

3.2. Resolution

The resolution of image (16) is determined by the region Ξ_y of integration in (25), which is the set of $\boldsymbol{\xi}$ defined by (21) as τ and β range over the subset of the data collection region $[\tau_{\min}, \tau_{\max}] \times [\beta_{\min}, \beta_{\max}]$ that is relevant at the point $\boldsymbol{y}_T$. In particular, the region Ξ_y is also restricted by the beam pattern W: the maximum X of $x = |y_1 - v\tau|$ is the distance along the

flight path for which the point $\boldsymbol{y}$ remains in the beam. Thus x is in the interval $[-X, X]$ where $X = vT$ with T being half the persistence interval.

Since $\beta = \omega_0 t' = \omega_0(t-\tau)$, the length of the interval $[\beta_{\min}, \beta_{\max}]$ is 2π times the number of cycles in our time window. We write $\beta_{\min} = -\Omega$ and $\beta_{\max} = \Omega$. We assume that the antenna beam is directed to the left of the flight path, so that $y_2 > 0$.

The boundary of the region Ξ is formed by the four curves $\mathcal{C}_\Omega, \mathcal{C}_{-\Omega}, \mathcal{C}_X, \mathcal{C}_{-X}$:

$$\begin{aligned} \mathcal{C}_{\pm\Omega} &= \{(\xi_1, \xi_2(x)) : \xi_1 = \pm a\Omega, \xi_2 = \pm\Omega b x, x \in [-X, X]\} \\ \mathcal{C}_{\pm X} &= \{\boldsymbol{\xi}(\beta) = (a, \pm Xb)\beta : \beta \in [-\Omega, \Omega]\} \end{aligned} \tag{26}$$

where we have written $a = 2(v/c)\left(y_2^2 + H^2\right)^{-1/2}$ and $b = -2(v/c)y_2\left(y_2^2 + H^2\right)^{-3/2}$.

We see that for a given target location (y_1, y_2), the curves $\mathcal{C}_{\pm\Omega}$ are vertical lines (in which only ξ_2 varies). Similarly, the curves $\mathcal{C}_{\pm X}$ are radial lines through the origin. The region $\Xi_{\boldsymbol{y}}$ is thus a bowtie. The size of $\Xi_{\boldsymbol{y}}$ depends not only on the target location (y_1, y_2) but also on the system parameters v, H, ω_0.

To obtain the point spread function (ambiguity function) for a particular image point $(0, y_2)$, we calculate the right-hand side of (25). We write $\boldsymbol{p} = \boldsymbol{z}_T - \boldsymbol{y}_T$ in (25) and change variables from $\boldsymbol{\xi} = (a, bx)\beta$ to (x, β), obtaining

$$K_{\boldsymbol{y}}(\boldsymbol{p}) = \frac{1}{(2\pi)^2}\int_{\Xi_{\boldsymbol{y}}} \mathrm{e}^{\mathrm{i}\boldsymbol{p}\cdot\boldsymbol{\xi}}\,\mathrm{d}\boldsymbol{\xi} = \frac{1}{(2\pi)^2}\int_{-\Omega}^{\Omega}\int_{-X}^{X} \mathrm{e}^{\mathrm{i}(a,bx)\cdot\boldsymbol{p}\beta}\left|\frac{\partial\boldsymbol{\xi}}{\partial(\beta, x)}\right|\mathrm{d}x\,\mathrm{d}\beta. \tag{27}$$

The Jacobian $|\partial\boldsymbol{\xi}/\partial(\beta, x)|$ is easily found to be equal to $|ab\beta|$; K can be calculated as follows:

$$\begin{aligned} K_{\boldsymbol{y}}(\boldsymbol{p}) &= \frac{-1}{(2\pi)^2}\left(\int_{-\Omega}^{0}\int_{-X}^{X} \mathrm{e}^{\mathrm{i}(a,bx)\cdot\boldsymbol{p}\beta} ab\beta\,\mathrm{d}x\,\mathrm{d}\beta - \int_{0}^{\Omega}\int_{-X}^{X} \mathrm{e}^{\mathrm{i}(a,bx)\cdot\boldsymbol{p}\beta} ab\beta\,\mathrm{d}x\,\mathrm{d}\beta\right) \\ &= \frac{a}{(2\pi)^2\mathrm{i}p_2}\left(\frac{\mathrm{e}^{\mathrm{i}(a,bX)\cdot\boldsymbol{p}\Omega} - 1}{\mathrm{i}(a, bX)\cdot\boldsymbol{p}} - \frac{\mathrm{e}^{\mathrm{i}(a,-bX)\cdot\boldsymbol{p}\Omega} - 1}{\mathrm{i}(a, -bX)\cdot\boldsymbol{p}}\right. \\ &\quad \left. - \frac{1 - \mathrm{e}^{-\mathrm{i}(a,bX)\cdot\boldsymbol{p}\Omega}}{\mathrm{i}(a, bX)\cdot\boldsymbol{p}} + \frac{1 - \mathrm{e}^{-\mathrm{i}(a,-bX)\cdot\boldsymbol{p}\Omega}}{\mathrm{i}(a, -bX)\cdot\boldsymbol{p}}\right) \\ &= \frac{a}{\pi^2 p_2}\left(\frac{\sin^2((a, bX)\cdot\boldsymbol{p}\Omega/2)}{(a, bX)\cdot\boldsymbol{p}} - \frac{\sin^2((a, -bX)\cdot\boldsymbol{p}\Omega/2)}{(a, -bX)\cdot\boldsymbol{p}}\right). \end{aligned} \tag{28}$$

Down-range resolution. Down-range resolution is obtained by setting $p_1 = 0$ in (28):

$$K_{\boldsymbol{y}}(0, p_2) = \frac{a}{\pi^2 p_2}\left(\frac{\sin^2(\Omega bXp_2/2)}{bXp_2} - \frac{\sin^2(-\Omega bXp_2/2)}{-bXp_2}\right) \propto \frac{\sin^2(\Omega bXp_2/2)}{(\Omega bXp_2/2)^2}, \tag{29}$$

where we have used $\sin^2 A = \sin^2(-A)$. From the right-hand side of (29), we see that the down-range resolution is

$$\Delta p_2 = \frac{4\pi}{\Omega bX} = \frac{2\pi c\left(y_2^2 + H^2\right)^{3/2}}{\Omega X v y_2}, \tag{30}$$

where the resolution is defined as the width of the central lobe of (29). We see that the down-range resolution is improved by taking a larger synthetic aperture $2X$; this is consistent with our expectation that a single Doppler measurement will provide no range information. Range information is obtained only from combining measurements across the synthetic aperture.

For $\omega_0 = 2\pi \times 100$ MHz, $v = 8\ \mathrm{m\,s^{-1}}$, a 0.5 s time window and $y_2 = 400$, the down-range resolution is roughly $\Delta p_2 \approx 80$ m.

Cross-range resolution. Cross-range or azimuthal resolution is obtained by calculating the $p_2 \to 0$ limit of (28) ; this can be done by means of l'Hospital's rule:

$$\begin{aligned}\lim_{p_2\to 0} K_y(p_1, p_2) &\propto \frac{\sin(\Omega a p_1/2)\cos(\Omega a p_1/2)}{\Omega a p_1/2} - \frac{\sin^2(\Omega a p_1/2)}{2(\Omega a p_1/2)^2} \\ &= \frac{1}{\Omega a p_1}\left[\sin(\Omega a p_1) - \frac{\sin^2(\Omega a p_1/2)}{\Omega a p_1/2}\right] \\ &= \frac{1}{\Omega a p_1}\frac{\sin(\Omega a p_1)}{\Omega a p_1}\left[\Omega a p_1 - \frac{1-\cos(\Omega a p_1)}{\sin(\Omega a p_1)}\right] \\ &= \frac{1}{\Omega a p_1}\frac{\sin(\Omega a p_1)}{\Omega a p_1}\left[\Omega a p_1 - \tan(\Omega a p_1/2)\right]. \end{aligned} \tag{31}$$

The width of the central lobe of $K_y(p_1, 0)$ is an estimate of the cross-range resolution and the first zero, which arises from the term in brackets in the last line of (31), involves solving the transcendental equation $\alpha - \tan(\alpha/2) = 0, \alpha \neq 0$. We obtain $\alpha = 2.33\ldots$, and so the cross-range resolution is

$$\Delta p_1 \approx \frac{2 \times 2.33}{\Omega a} = \frac{2.33c\left(y_2^2 + H^2\right)^{1/2}}{\Omega v}. \tag{32}$$

For the same parameter values given above, the cross-range resolution is roughly $\Delta p_1 \approx 100$ m.

We see that both down-range and cross-range resolutions are improved by having a larger number of wave cycles within the time window (i.e., by increasing the frequency ω_0 or using a longer time window) and increasing the flight velocity v. Resolution is worse for points more distant from the flight path.

3.3. Numerical implementation

A full implementation of the scheme in section 3.1 is, computationally, very expensive. Equation (16) is a triple integral with kernel B given by equation (24). Moreover, evaluation of this filtering kernel requires calculation of A (equation (11)) and the Jacobian (equation (23)). Even with the use of look-up tables, the computation requirements associated with such spatially-varying kernels can be daunting.

Instead, we make use of our previous observation: the leading-order contribution to η comes from the critical set $\partial\phi/\partial\beta = 0$ which, in this approximation, is a straight line in the $\tilde{\mu}$–τ plane. Consequently, an alternative approach can be based on identifying the straight line components in $\eta(\tau, \tilde{\mu})$.

An efficient line-detection algorithm makes use of the Radon–Hough transform that integrates over all possible lines:

$$\mathcal{H}\{\eta\}(d, \theta) = \iint \eta(\tau, \tilde{\mu})\delta(d - \tau\cos\theta - \tilde{\mu}\sin\theta)\,\mathrm{d}\tau\,\mathrm{d}\tilde{\mu}. \tag{33}$$

The transform-image of η yields a detected (matched) line's perpendicular offset from the origin d and the angle θ of this offset. The offset d and angle θ are related to the slope m and τ-intercept b via $d = b\cos\theta$ and $m = \tan\theta$. Because τ has the dimensions of time, m has the

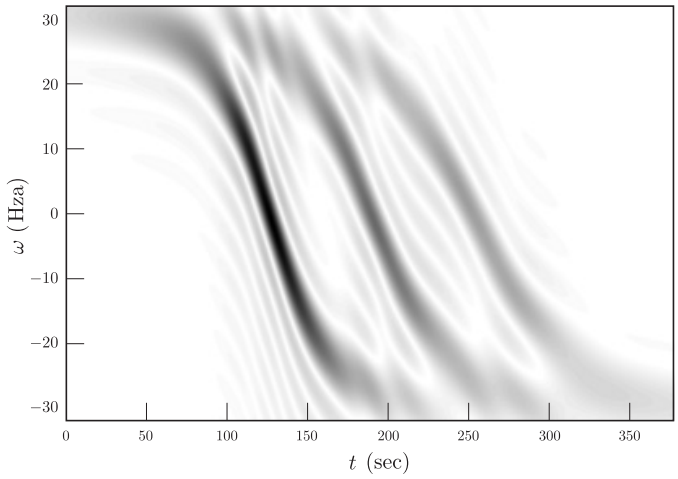

Figure 3. The Doppler return from three point scatterers.

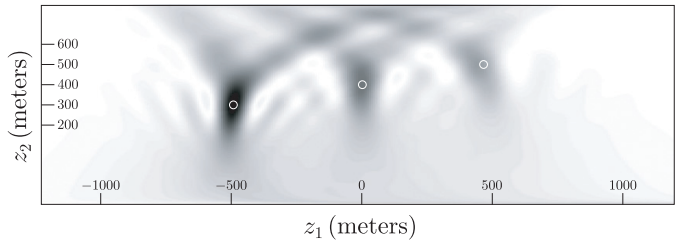

Figure 4. The (resampled) Radon–Hough transform of the data in figure 3. The true locations are marked by ○; the flight path is along the z_1 axis.

dimensions of reciprocal time. These dimensional quantities are related to the dimensionless $\tilde{\tau}$-intercept $\tilde{b}$ and slope $\tilde{m}$ of the line in the $\tilde{\mu}$–$\tilde{\tau}$ plane via $\tilde{b} = vb/H$ and $\tilde{m} = Hm/v$. According to our analysis above, we can therefore form the estimates

$$z_1 = \frac{vd}{\cos\theta} \qquad \text{and} \qquad \cot\theta = \frac{H}{v}\left(\frac{-c}{2v}\right)\sqrt{\left(\frac{z_2}{H}\right)^2 + 1}$$

$$\Rightarrow \quad z_2 = \frac{1}{H}\sqrt{\frac{4v^3\cot^2\theta}{H^2c^2} - 1} \tag{34}$$

to locate the scattering centre. Our expedient imaging scheme is therefore performed as a two-step process: (1) form the Radon–Hough transform $\mathcal{H}\{\eta\}(d,\theta)$ of the correlation data; and (2) map (resample) according to equation (34).

Figure 3 shows the (magnitude of the) Doppler frequency response of three isolated equal-strength scatterers as a function of time. (The difference in relative strength of each curve is due to a difference in scatterer range.) The simulated data were constructed under the model assumptions of a straight flight path for the radar with transmit frequency of $\omega_0 =$ 100 MHz and relative velocity of 8 m s^{-1}. Each data point was determined from a 0.5 s modelled measurement interval (according to equation (13)).

Figure 4 was formed from the data of figure 3 by resampling the Radon–Hough transform according to equation (34). The figure displays the magnitude of the simple transform and no

attempt has been made to correct for range-dependent magnitude errors—although this next image processing step could be easily made once the individual scatterer locations have been determined. Figure 4 could be improved by image-processing techniques such as high-pass filtering or thresholding. We leave this topic for the future.

We note that figure 4 shows a superposition of three point-spread functions for our expedient imaging scheme.

4. Conclusions and future work

We have developed a mathematical model for the radar return signal resulting from a transmitted CW waveform in the case of an antenna moving above a scattering surface. For the case of a flight path with constant velocity over a flat surface, we have also developed two imaging algorithms. Finally, we have displayed the results of numerical simulation for a simple case.

CW radar is attractive for a variety of reasons including simplicity of hardware design and data analysis. For monostatic systems, however, the issue of direct coupling between the co-located transmitter and receiver can be significant and transmitted energy 'spillover' into the receiver can mask detection of weak targets. Isolating these two radar components in CW-Doppler systems is an area of ongoing engineering development [19] and current capabilities restrict the practical implementation of this imaging method to specialized situations. Of course, this problem is not generally manifest in bistatic systems for which the transmitter and receiver are widely separated and our analysis can be readily modified to include such radar configurations.

Much more work remains to be done, especially for cases in which the geometry is more complicated. In addition we leave for the future the problem of developing fast numerical implementations [16] of the general imaging formula.

Acknowledgments

This work was supported by the Office of Naval Research, the Air Force Office of Scientific Research under agreement F49620-03-1-0051, and by the Air Force Research Laboratory[3] appunder agreement FA87500308276. This work was also supported in part by Rensselaer Polytechnic Institute, by the NSF-supported UCLA Institute for Pure and Applied Mathematics and by the NSF Focused Research Groups in the Mathematical Sciences program.

References

[1] Andersson L-E 1988 On the determination of a function from spherical averages *SIAM J. Math. Anal.* **19** 214–32
[2] Agranovsky M and Quinto E T 1996 Injectivity sets for the Radon transform over circles and complete systems of radial functions *J. Funct. Anal.* **139** 383–414
[3] Borden B 1999 *Radar Imaging of Airborne Targets* (Bristol: Institute of Physics Publishing)
[4] Borden B 2002 Mathematical problems in radar inverse scattering *Inverse Problems* **18** R1–28
[5] Chen V C and Ling H 2002 *Time-Frequency Transforms for Radar Imaging and Signal Analysis* (Boston, MA: Artech House Publishers)
[6] Cook C E and Bernfeld M 1967 *Radar Signals* (New York: Academic)

[3] Consequently the US Government is authorized to reproduce and distribute reprints for Governmental purposes notwithstanding any copyright notation thereon. The views and conclusions contained herein are those of the authors and should not be interpreted as necessarily representing the official policies or endorsements, either expressed or implied, of the Air Force Research Laboratory or the US Government.

[7] Hellsten H and Andersson L-E 1987 An inverse method for the processing of synthetic aperture radar data *Inverse Problems* **3** 111–24
[8] Herman G T, Tuy H K, Langenberg K J and Sabatier P C 1988 *Basic Methods of Tomography and Inverse Problems* (Philadelphia, PA: Hilger)
[9] Klemm R 2002 *Principles of Space-Time Adaptive Processing* (Cornwall: The Institution of Electrical Engineeers)
[10] Langenberg K J, Brandfass M, Mayer K, Kreutter T, Brüll A, Felinger P and Huo D 1993 Principles of microwave imaging and inverse scattering *EARSeL Adv. Remote Sens*. **2** 163–86
[11] Louis A and Quinto E T 2000 Local tomographic methods in SONAR *Surveys on Solution Methods for Inverse Problems* ed D Colton, H W Engl, A K Louis, J R McLaughlin and W Rundell (New York: Springer)
[12] Maass P 1989 Wideband radar: the hyp transform *Inverse Problems* **5** 849–57
[13] Mensa D L 1981 *High Resolution Radar Imaging* (Dedham, MA: Artech House)
[14] Natterer F 1986 *The Mathematics of Computerized Tomography* (New York: Wiley)
[15] Natterer F and Wübbeling F 2001 *Mathematical Methods in Image Reconstruction* (Philadelphia, PA: SIAM)
[16] Nilsson S 1997 Application of fast backprojection techniques for some inverse problems of integral geometry *Linköping Studies in Science and Technology* Dissertation no. 499 Linköping University, Sweden
[17] Nolan C J and Cheney M 2002 Synthetic aperture inversion *Inverse Problems* **18** 221–36
[18] Roulston M S and Muhleman D O 1997 Synthesizing radar maps of polar regions with a Doppler-only method *Appl. Opt*. **36** 3912–9
[19] Saunders W K 1990 CW and FM radar *Radar Handbook* ed M I Skolnik (New York: McGraw-Hill)
[20] Skolnik M I 1980 *Introduction to Radar Systems* (New York: McGraw-Hill)
[21] Stutzman W L and Thiele G A 1998 *Antenna Theory and Design* 2nd edn (New York: Wiley)
[22] Son J S, Thomas G and Flores B C 2001 *Range-Doppler Radar Imaging ad Motion Compensation* (Boston, MA: Artech House)
[23] Sullivan R J 2000 *Microwave Radar Imaging and Advanced Concepts* (Boston: Artech House)
[24] Tsang L, Kong J A and Shin R T 1985 *Theory of Microwave Remote Sensing* (New York: Wiley)